Classification of ocean surface slicks in simulated hybrid-polarimetric SAR data

Arnt-Børre Salberg, *Member*, and Siri Øyen Larsen

Abstract—In this paper, we consider hybrid-polarimetric SAR data of ocean surface slicks, and hypothesize that we can design a system that is able to discriminate between mineral oil, plant oil and clean sea. We focus particularly on challenges related to dataset shift between training and test data. In SAR images of ocean surfaces, dataset shift is typically caused by variation of wind level and incident angles that directly impact the backscatter intensities. We evaluate several classifiers, domain adaptation strategies and multilooking strategies. Hybrid-polarimetric SAR data are simulated from the Radarsat-2 quad-pol images. The proposed methodology was trained using five different Radarsat-2 quad-pol images that cover slicks of known types, and tested on 10 different Radarsat-2 quad-pol images covering various ocean surface slicks. The results show that we were able, to a large degree, to classify the type of various surface slicks. The average classification accuracy obtained from cross-validation on the training data was 91%. The results also show that we were able to correctly classify surface slick in new test images, even if the wind, surface and acquisition conditions were different from the training images. We conclude that hybrid-polarity is an attractive mode for future enhanced SAR-based oil spill monitoring; however, to fully exploit the imaging mode single-look complex images are necessary.

I. INTRODUCTION

Pollution by oil spills from ships or offshore installations in open sea and coastal waters, whether accidental or deliberate, is a major problem due to frequent transport of goods by ships, and represents a serious threat to the marine environment.

Operational oil spill monitoring is currently done using a combination of satellite monitoring and aircraft surveillance. The combined use of satellite-based synthetic aperture radar (SAR) images and aircraft surveillance flights is a cost-effective way to monitor oil spills in large ocean areas and contribute to identify and prosecute the culprits. SAR images cover large areas, but aircraft observations are needed to prosecute the polluter, and in certain cases to verify the oil spill.

The SAR image values are related to sea microwave backscattering. For clean sea surfaces, Bragg scattering is dominant for incident angles between about 20° and 70° [1]. When oil is spilled on the sea surface, it will spread to form a thin layer on the water surface. This layer will dampen waves on the ocean surface, and thereby cause dark patches in the SAR image. However, even though SAR is well suited for detection of oil spills on the sea surface, a major challenge of SAR based oil spill detection is to distinguish oil spills from

Salberg and Larsen are with the Norwegian Computing Center, Dept. SAMBA, Section for Earth Observation, P.O. Box 114 Blindern, NO-0314 Oslo, Norway. Corresponding author A. B. Salberg, tel: +47 93 02 34 23, fax: +47 22 69 76 60, e-mail: `salberg@nr.no`

other natural phenomena that dampen the waves and create dark patches on the surface (natural dark patches are termed oil spill look-alikes). Typically, look-alikes arise from natural films/slicks, grease ice, low wind areas, wind sheltering by land, rain cells, shear zones, internal waves, etc. [1].

The SAR images used for operational oil spill monitoring have mainly been based on single polarization data, for example, transmitting vertically polarized radiation and receiving vertical polarization (VV single-pol systems). Dual-polarized SAR that transmits on either H- or V-polarization and receives both H- and V-polarization (i.e. VV/VH or HH/HV) are supported by many SAR systems, and for sensors like Radarsat-2 and Sentinel-1, dual polarization provides the same spatial coverage as single-polarized SAR data [2]. However, since the co-polarized and cross-polarized channels are often uncorrelated (due to the reflection symmetry hypothesis) for sea surfaces where Bragg-scattering is considered to be dominant [3], the phase difference between the co- and cross-polarized channels is not useful for many maritime applications. This is not the case for the correlation between the phase for two co-polarized channels HH and VV (see e.g. [4], [5]).

During the last decade both coherent dual-pol and quad-pol SAR configurations have been investigated in several oil spill detection studies [4], [5], [6], [7], [8], [9], [10], [11], [12]. In many of these studies it has been demonstrated that the use of polarimetric SAR increases the oil spill detection performance, and makes it possible to discriminate oil slicks from biogenic slicks [4], [8], [13]. It is in particular the co-polarized phase difference between the VV and HH channels that provides additional discrimination power to the oil spill detection problem [4]. The studies have included data from several platforms, including SIR-C data (L- and C-band) obtained by the space shuttle in April and October 1994 [6], [4], ALOS PalSAR (L-band) [9], Radarsat-2 quad-pol (C-band) [10], [11], and TerraSAR-X dual-pol VV/HH (X-band) [5] SAR data. Characterization of oil slicks in terms of oil type has also been investigated, both for quad-pol Radatsat-2 data [14], [15], [16] and TerraSAR-X data [15], [16]. These studies considered a variety of multi-polarization features and demonstrated the potential of using multi-polarization SAR data to estimate the oil type.

The major limitation of the available quad-pol and coherent dual-pol VV/HH SAR data is the reduced swath width and constrained span of incidence angle that make quad-pol and coherent dual-pol modes less appropriate for routine large-scale coverage. The quad-pol mode on Radarsat-2 has only a spatial coverage of 25 km × 25 km (nominal swath width of 25 km). The VV/HH dual-pol is only available for Stripmap mode

on TerraSAR-X, which has a small swath width of 15 km and a nominal length of 50 km. The first generation of the X-band Cosmo-SkyMed provides only a non-coherent polarimetric mode. Envisat ASAR also offered a mode for dual-pol VV/HH SAR data, but the transmission of this mode was based on an alternating polarization scheme with no option for obtaining information about the co-polarized phase difference.

Due to these reduced capabilities for operational oil spill monitoring using dual-pol VV/HH or quad-pol SAR data, the possibilities of using compact polarimetry for oil spill detection has been investigated by simulating compact polarization from Radarsat-2 quad-pol SAR data [10], [17], [18]. Compact polarimetry is a name for SAR schemes in which a single polarimetric electromagnetic signal is transmitted, and two orthogonal polarimetric electromagnetic signals are received (which for convenience we denote to be the H and V channel signals), together with their relative phase. However, compact polarimetry differs from conventional dual-pol schemes since it relies on transmitting the H- and V-polarization simultaneously, and not either H or V. For an introduction to compact polarimetry we refer the reader to [19], [20], [21].

The objective of compact polarimetry is to realize many (but not all) benefits of quad-polarization or dual-polarization HH/VV, without the reduced swath width [19]. Several compact polarimetry modes are possible. The $\pi/4$-mode transmits a linear polarized field rotated at 45° ($H + V$) and receives coherently in both the H and V channels [22]. In the circular polarization mode the SAR instrument transmits either a right or left circular polarized field ($H \pm i \cdot V$, where $+$ and $-$ denote left and right circular polarization, respectively, and i denotes the complex identity), and receives in both the right and the left circular polarized channels [19]. The "hybrid" compact mode transmits circular polarization and receives in the two orthogonal linear polarizations H and V [23]. Among these three compact polarimetry modes, the latter has been ranked to be the most promising in terms of performance and receiver complexity [19].

One of the major motivations for considering compact polarimetry for oil spill detection is that, in addition to the SAR satellites Risat-1 (India) and the experimental compact polarity mode on the ALOS-2 PALSAR-2 (Japan), the planned Radarsat Constellation Mission (Canada) will provide a compact polarimetry mode. Both Risat-1 and the Radarsat Constellation Mission support the hybrid-polarimetric mode with transmission of right circular polarized waves, and coherent reception in the H and V channels. The coming Radarsat Constellation Mission will be particularly tailored to maritime applications by offering e.g. a compact polarimetry mode with a swath width of 350 km and a resolution of 50 m, or a low noise mode with the same swath width and a resolution of 100 m. Such spatial coverage is well suited for large scale oil spill monitoring, and will provide new capabilities in terms of reduced false alarm rate and increased oil spill discrimination.

In SAR-based oil spill detection, only a few studies have considered compact polarimetry [10], [17], [18], [24], [25]. Zhang et al. [10] considered the hybrid polarization mode, and showed that the conformity coefficient, derived from the compact polarimetry data simulated from Radarsat-2 quad-pol SAR data, may be applied to discriminate oil spills from look-alikes. The methodology was successfully demonstrated on a Radarsat-2 quad-pol image covering oil spills from the Deepwater Horizon incident. Shirvany et al. [18] demonstrated that the degree of polarization provided valuable information for man-made object and oil slick detection under different polarizations and incident angles. Compact polarimetry has also been applied to other ocean applications, like ship detection [26] and iceberg detection [27]. Salberg et al. [17], Buono et al. [24] and Kumar et al. [25] studied the oil spill detection performance of several measures in hybrid-polarimetric SAR images, where Kumar et al. [25] is one of the few works that have used real hybrid-polarimetric data (from the Risat-1 satellite), i.e., not simulated hybrid-polarimetric data.

During the last years, substantial research has been done on developing methods for detection and monitoring of oil spill at sea in synthetic aperture radar (SAR) images [28]. However, operational services like EMSA's CleanSeaNet does not currently provide the user with estimates of oil spill characteristics, like type or thickness. The knowledge of oil type is critical with respect to the measures to be initiated in clean-up operations.

In this paper, we consider hybrid-polarimetric SAR data, and hypothesize that we may train a system to distinguish between mineral oil, plant oil and clean sea. We will use this trained system to classify new images, in new areas. We will in particular focus on challenges related to dataset shift between training and test data. In SAR images of ocean surface, dataset shift is typically caused by variation of wind level and incident angles that directly impact the backscatter intensities. We compare several domain adaptation strategies to handle the dataset shift problem.

II. Theory

In this section, we describe the proposed system, and the underlying theory, for ocean slick classification in hybrid-polarimetric SAR data.

A. Radar backscatter from the ocean surface

We model the ocean surface using a composition of slightly rough and tilted facets [29]. In this model, each facet is a Bragg scatterer that models small-scale surface roughness, with heights that are small compared to the radar wavelength and randomly distributed on the scattering surface [29], [30]. Larger scale gravity waves are modelled by the tilt of each facet, and result in cross-polarized backscattered signals. Since the tilted facet model includes both small-scale surface roughness and large scale gravity waves, we refer to it as a two-scale scattering model.

In the two-scale scattering model, the orientation of the facet normal is defined by two angles ψ' and ξ' [29]. The angle ψ' denotes the angle between the vertical and the projection of the tilted facet's normal onto the scattering plane, whereas the angle ξ' denotes the angle between the vertical and the projection of the tilted patch's normal onto the plane

perpendicular to the scattering plane (along-track plane for the case of broadside imaging geometry) [30].

The two-scale scattering model results in the following equations for the normalized radar cross-section is [29], [30]

$$\sigma_{xx}^0 = 4\pi k_r^4 \cos^4 \theta_i$$
$$\left| \left(\frac{\sin(\theta + \psi')\cos\xi'}{\sin\theta_i} \right)^2 B_{xx}(\theta_i) + \left(\frac{\sin\xi'}{\sin\theta_i} \right)^2 B_{yy}(\theta_i) \right|^2$$
$$\times W \left(2k_r \sin(\theta + \psi'), 2k_r \cos(\theta + \psi') \sin\xi' \right) \quad (1)$$

$$\sigma_{xy}^0 = 4\pi k_r^4 \cos^4 \theta_i$$
$$\left(\frac{\sin(\theta + \psi')\sin\xi'\cos\xi'}{\sin^2\theta_i} \right)^2 |B_{yy}(\theta_i) - B_{xx}(\theta_i)|^2$$
$$\times W \left(2k_r \sin(\theta + \psi'), 2k_r \cos(\theta + \psi') \sin\xi' \right), \quad (2)$$

where the subscripts x and y denote either H or V polarization, θ is the local incident angle relative to the local untilted up, $\theta_i = \cos^{-1}[\cos(\theta + \psi')\cos(\xi')]$ is the local angle of incidence, $W(\cdot)$ is the 2-D wavenumber spectral density of the ocean surface roughness, k_r is the radar wavenumber in free space, and the Bragg scattering coefficients are given by [30]

$$B_{HH} = \frac{\cos\theta_i - \sqrt{\epsilon - \sin^2\theta_i}}{\cos\theta_i + \sqrt{\epsilon - \sin^2\theta_i}} \quad \text{and} \quad (3)$$

$$B_{VV} = \frac{(\epsilon - 1)(\sin^2\theta_i - \epsilon(1 + \sin^2\theta_i))}{\left(\epsilon \cos\theta_i + \sqrt{\epsilon - \sin^2\theta_i} \right)^2}. \quad (4)$$

The angles ψ' and ξ' are not tilt angles defined in terms of in-plane and out-of-plane tilts, but seem to be rotation angles [31]. Let ψ and ξ denote in-plane (range slope) and out-of-plane (azimuth slope) tilt angles, respectively. The angles ψ' and ξ' may then be expressed as $\tan\xi' = -\tan\xi\cos\psi$ and $\psi' = \psi$ [31].

The facet tilt causes a rotation of the local plane of incidence around the look direction by an angle ϕ. This is related to the facet in-plane and out-of-plane tilt angles ψ and ξ and the global incident angle θ by [32], [33]

$$\tan\phi = \frac{\tan\xi}{-\tan\psi\cos\theta + \sin\theta}. \quad (5)$$

Using this relationship, the normalized radar cross-section in Eq. (1) and (2) may be expressed as

$$\sigma_{xx}^0 = 4\pi k_r^4 \cos^4 \theta_i \left| \cos^2\phi B_{xx}(\theta_i) + \sin^2\phi B_{yy}(\theta_i) \right|^2$$
$$\times W \left(2k_r \sin(\theta + \psi), 2k_r \cos(\theta + \psi) \sin\xi' \right) \quad (6)$$

$$\sigma_{xy}^0 = 4\pi k_r^4 \cos^4 \theta_i \left(\sin\phi \cos\phi \right)^2 |B_{yy}(\theta_i) - B_{xx}(\theta_i)|^2$$
$$\times W \left(2k_r \sin(\theta + \psi), 2k_r \cos(\theta + \psi) \sin\xi' \right), \quad (7)$$

where $\sin\xi'$ may be expressed as

$$\sin\xi' = \frac{-\sin(\theta - \psi)\tan\phi}{\pm\sqrt{1 + \sin^2(\theta - \psi)\tan^2\phi}}.$$

For a more complete description of the influence of the ocean waves dynamics, like velocity bunching, on the SAR imaging properties we refer the reader to e.g. [34].

B. Hybrid-polarimetric coherency matrix

The Sinclair scattering matrix $\mathbf{S} = [S_{xy}] \in \mathbb{C}^{2\times2}$ is a matrix of scattering coefficients, where S_{xy} is a scattering coefficient corresponding to receive polarization x and transmit polarization y. Please note that for a given frequency and scattering geometry, $\mathbf{S}$ depends only on the scattering properties of the target.

Let B_{HH} and B_{VV} denote the Bragg scattering coefficients for horizontal and vertical polarizations, respectively. The Sinclair matrix of the two-scale scattering model may then be expressed as [33]

$$\mathbf{S} = a_s \mathbf{R}(\phi) \begin{bmatrix} B_{HH}(\theta_i) & 0 \\ 0 & B_{VV}(\theta_i) \end{bmatrix} \mathbf{R}^T(\phi), \quad (8)$$

where the coefficient $|a_s|^2 = k_r^4 \cos^4\theta_i W(\cdot)$ and the rotation matrix $\mathbf{R}(\phi)$ is given as

$$\mathbf{R}(\phi) = \begin{bmatrix} \cos\phi & \sin\phi \\ -\sin\phi & \cos\phi \end{bmatrix}. \quad (9)$$

Under the two-scale Bragg scattering model and right circular transmit, linear receive (CL) mode, the hybrid-polarimetric scattering coefficients may be expressed as

$$E_H = (S_{HH} - iS_{HV})/\sqrt{2} \quad (10)$$
$$= \frac{a_s}{\sqrt{2}}[B_{HH}\cos^2\phi + B_{VV}\sin^2\phi$$
$$+ i(B_{HH} - B_{VV})\cos\phi\sin\phi]$$

$$E_V = (S_{VH} - iS_{VV})/\sqrt{2} \quad (11)$$
$$= \frac{a_s}{\sqrt{2}}[-iB_{HH}\sin^2\phi - iB_{VV}\cos^2\phi$$
$$- (B_{HH} - B_{VV})\cos\phi\sin\phi].$$

By considering the following quantities [17]

$$E_H + iE_V = \frac{1}{\sqrt{2}}(S_{HH} + S_{VV}) = \frac{a_s}{\sqrt{2}}(B_{HH} + B_{VV}), \quad (12)$$

$$E_H - iE_V = \frac{1}{\sqrt{2}}(S_{HH} - S_{VV} - 2iS_{HV})$$
$$= \frac{a_s}{\sqrt{2}}(B_{HH} - B_{VV})\exp(i2\phi), \quad (13)$$

we observe that $E_H + iE_V$ is independent of the rotation angle ϕ and $E_H - iE_V$ only depends on ϕ via the complex exponential $\exp(i2\phi)$. Using these quantities, the corresponding measured compact polarimetric coherency matrix may be expressed as

$$\mathbf{D} = \begin{bmatrix} D_{11} & D_{12} \\ D_{12}^* & D_{22} \end{bmatrix}. \quad (14)$$

where

$$D_{11} = \langle|E_H + iE_V|^2\rangle = \frac{1}{2}\langle|a_s|^2|B_{HH} + B_{VV}|^2\rangle \quad (15)$$

$$D_{22} = \langle|E_H - iE_V|^2\rangle = \frac{1}{2}\langle|a_s|^2|B_{HH} - B_{VV}|^2\rangle \quad (16)$$

$$D_{12} = \langle(E_H + iE_V)(E_H - iE_V)^*\rangle$$
$$= \frac{1}{2}\langle|a_s|^2(B_{HH} + B_{VV})(B_{HH} - B_{VV})^*\exp(-i2\phi)\rangle, \quad (17)$$

$$\mathbf{D} \approx |a_s|^2 \begin{bmatrix} |B_{HH} + B_{VV}|^2 & e^{-i2\phi}(B_{HH} + B_{VV})(B_{HH} - B_{VV})^* \\ e^{i2\phi}(B_{HH} + B_{VV})^*(B_{HH} - B_{VV}) & |B_{HH} - B_{VV}|^2 \end{bmatrix}. \tag{18}$$

C. Domain adaptation

One of the major challenges in data analysis is that many of the available analysis methods only work well when the training and test data are drawn from the same features space, and the same statistical distribution. When the data distribution changes, most statistical and machine learning methods need to be rebuild using new training data. In many remote sensing applications, this is difficult due to costs and near real time requirements [36]. Many researchers has therefore investigated methods that adapt the analysis methods from the training data domain to the test data domain (*domain adaptation*), and thereby reducing the need and effort to recollect training data [36].

In remote sensing, domain adaptation has received increased attention over the last decades [36], [37], [38], [39], and it has been demonstrated that, under some conditions, it is possible to adapt or adjust the training and/or test data, such that their data distributions are similar.

When using SAR images for detection and classification of ocean surface slicks, there are several factors that contribute to the background backscattering level from clean sea ocean surfaces. Two of the most important ones are the wind level and incidence angle, as emphasised by Skrunes et al. [40]. They evaluated the use of log-cumulants of dual-pol data as a means to distinguish various oil types, but normalized the log-cumulants such that their value for clean sea was zero.

III. OCEAN SLICK CLASSIFICATION

The wind speed has a major impact on the intensity of the radar backscatter from ocean surfaces, and in order to design an effective oil spill classification system, methods that handle the varying backscatter intensities between the SAR images are needed. The proposed system reduces the effect of wind and varying incidence angle by aligning the data distribution of each feature for clean sea areas, and thereby adjusting the domain of the test data to the data distribution of the training data.

The proposed pixel-based ocean slick classification scheme consists of the following steps: (1) feature extraction (2) automatic extraction of clean sea samples, (3) domain adaptation, (4) classification and (5) confidence estimation.

A. Feature extraction

As a pre-processing step we correct for varying incidence angles by dividing the received signal E_H and E_V with $\tan^2 \theta_R / \tan^2 \theta_i$, where θ_i is the incidence angle and θ_R is a reference angle (i.e. the incidence angle at the center of the image).

The features considered in this study are the three elements of the hybrid-polarimetric coherency matrix: D_{11}, D_{22} and

$|D_{12}|$, the coherence measure, Coh [17], the m and $\sin 2\xi$ components of the $m - \xi$-decomposition [17], the conformity measure, μ [17], the α-angle in the H/α-decomposition [41], standard deviation of the co-polarized phase difference (CPD) [17], ϕ_{CPD}, and the covariance matrix $C_{HH} = \langle |E_H|^2 \rangle$, $C_{VV} = \langle |E_V|^2 \rangle$ and $\text{Re}\{C_{HV}\}$, $\text{Im}\{C_{HV}\}$, where $C_{HV} = \langle E_H E_V^* \rangle$.

Five different feature sets are considered:

- *Coherence*: The elements of the coherency matrix: D_{11}, D_{22} and $|D_{12}|$
- *Covariance*: The elements of the covariance matrix: C_{HH}, C_{VV} and $\text{Re}\{C_{HV}\}$, $\text{Im}\{C_{HV}\}$
- *Stokes*: The four elements of the Stokes vector: g_0, g_1, g_2 and g_3.
- *Extended*: A feature set consisting of D_{11}, D_{22}, $|D_{12}|$, Coh, m, $\sin 2\xi$, μ, α, and ϕ_{CPD}.
- *RH and RV*: The elements of the covariance matrix: C_{HH} and C_{VV}. These features correspond to the features provided by ground range detected (GRD) hybrid-polarimetric SAR data

B. Automatic extraction of clean-sea samples

The extraction of clean sea samples is based on the hypothesis that the SAR image consists of a large portion of clean sea pixels, and that these pixels have higher intensity values than the surface slicks.

We automatically extract feature samples from clean sea areas by assuming that, for the conformity measure μ, the main peak of the image histogram represents clean sea. I.e., we make the assumption that the majority of the imaged area is covered by clean sea. To locate clean sea pixels, we first apply the method by Kittler and Illingworth [42] to select a threshold x_{KI}. We then compute the histogram and locate its maximum x_{max} and 99% percentile x_{99}. We assume that all feature values between x_{KI} and x_{99} correspond to clean sea pixels. From these values we randomly sample $N = 1000$ feature values.

C. Domain adaptation

The extracted clean-sea pixel locations form the basis of the domain adaptation algorithm, in which they are used to construct a transform-function that transforms the feature values of the test image such that the clean sea backscatter intensity distribution matches the clean sea intensity distribution of the training images. There are several ways to construct such a function. We will evaluate three different approaches:

1) Normal transformation: Estimate a function that transforms the clean-sea pixels to a standard normal distribution $\mathcal{N}(0, 1)$. A similar strategy was applied by Storvik et al. [43] for multisensor fusion of optical and SAR images.

Let $\{x_i\}$, $i = 0, 1, \ldots, N - 1$ be a set of values for a given feature at clean-sea locations. Assume that the feature

values x are distributed according to the probability density function $f_{CS}(x)$, with a corresponding cumulative density function $F_{CS}(x)$. Then the transform-function of the feature values to $\mathcal{N}(0,1)$ is $\mathcal{T}(x) = F_N^{-1}(F_{CS}(x))$, where F_N is the cumulative density functions of $\mathcal{N}(0,1)$. Since F_{CS} is unknown, we estimate the data distribution of the clean-sea samples using the Parzen density estimate [44], i.e.

$$
\begin{aligned}
F_{CS}(x) &= \int_{-\infty}^{x} f_{CS}(\xi)\, d\xi \\
&= \int_{-\infty}^{x} \sum_{n=0}^{N-1} \frac{1}{\sqrt{2\pi}\sigma} \exp\left(\frac{\|\xi - x_n\|^2}{2\sigma^2}\right) d\xi, \quad (19)
\end{aligned}
$$

where σ is a smoothing parameter. We estimate the smoothing parameter using Silverman's rule [44]. The continuous function $\mathcal{T}(x)$ is applied to all pixels in the image, including surface slicks. In the transformed image the distribution for clean sea samples is now assumed to be $\mathcal{N}\{0,1\}$.

2) Mode scaling: Transform the data by multiplying all pixels in the test image with a feature dependent scaling factor α_f. The α_f scaling factor is selected such that the mode of the clean-sea distribution of each feature is 1.

3) Zero-mean, unit-variance transformation: The features are transformed such that the clean-sea distribution of each feature has zero mean and unit variance. This is achieved by subtracting the mean value and dividing by the standard deviation.

D. Classification and confidence level estimation

Let $c_i \in \{\omega_1, \omega_2, \ldots, \omega_C\}$ denote the class label for the ith pixel, where $\omega_1, \omega_2, \ldots, \omega_C$ denote the C different class categories. We will follow the approach by Solberg [45], and predict class labels $\mathbf{C} = \{c_1, c_2, \ldots, c_N\}$ of the scene, given the image of features $\mathbf{X} = \{\mathbf{x}_1, \mathbf{x}_2, \ldots, \mathbf{x}_N\}$, as the labels that maximizes $\log(P(\mathbf{X}|\mathbf{C}) + \log(P(\mathbf{C}))$. The data term $P(\mathbf{X}|\mathbf{C})$ will be modelled using either a random forest (RF) [46] or an extreme gradient boosting (XGBoost) [47] classifier, whereas the label term $P(\mathbf{C})$ will be modelled using a Markov random field [45].

The classifier categorizes all pixels in the image into the classes clean sea, lookalike, plant oil or mineral oil, where the mineral oil class is a merged class of emulsion and crude oil. To prevent spurious errors when classifying single pixels, we apply a Markov random field in order to introduce spatial information from neighboring pixels (see Sec. III-E).

1) Random forests classifier: A Random forests is an ensemble learning method for classification or regression that operate by constructing a multitude ($nTrees$) of decision trees at training time. Each decision tree is constructed from a random subset of the training data, and at each terminal node the split-point is estimated by considering a random subset of $mTry$ features. At test time, the output class is the mode of the classes predicted by the $nTrees$ individual trees. For more information about the random forests classifier, please see Hastie et al. [48].

The package `randomForest` in R (http://cran.r-project.org/web/packages/randomForest/) was used to implement the random forests classifier. The `mTry` parameter was determined using cross-validation, `nTrees` was set to 1001, and the class weights were set to $1/n_c$ where n_c is the number of samples in class c.

To estimate the confidence level, we propose to use the probability of the predicted class, given the data. For the random forests classifier, this probability may be estimated using the fraction of votes each class obtains for a given feature vector, i.e.

$$
P(\omega_k|\mathbf{x}) = \frac{n_k}{N}, \quad k = 1, \ldots, C, \quad (20)
$$

where $\mathbf{x} = [x_0, x_1, \ldots, x_{N-1}]^T$ denotes the feature vector, N is the total number of trees grown, n_k is the number of trees that classify $\mathbf{x}$ to class ω_k, and C denotes the number of classes. A similar approach was taken by Loosvelt et al. [49] in order to estimate the per-pixel uncertainty.

2) Extreme Gradient Boosting: XGBoost is a scalable end-to-end tree boosting system. It has an inherent regularization that helps to reduce overfitting, and implements parallel processing in order increase the processing speed. The XGBoost algorithm has many parameters that need to be determined, including the learning rate (eta), maximum depth of a tree ($maxDepth$), minimum sum of weights of all observations required in a child ($minChildWeight$), and minimum loss reduction required to make a split ($gamma$). The R-package Extreme Gradient Boosting (`xgboost`), (https://cran.r-project.org/web/packages/xgboost/) is used, with the parameters determined by cross-validation. The parameters are: $eta = 0.1$, $maxDepth = 8$, $minChildWeight = 1$, $gamma = 0$.

For more information about extreme gradient boosting please see Chen and Guestrin [47]. As for the random forests classifier, `xgboost` also provides the probability of the predicted class, which may be used as a confidence measure about the decision.

E. Markov random field modelling of spatial context

Since ocean slicks consist of more than one pixel, we consider models that use contextual information between neighboring pixels. More specifically, we apply a Markov random field to perform contextual image classification [45], [50], and model the class label prior for the ith pixel, given the neighboring pixels, as

$$
P(c_i|c_j; j \in \mathcal{N}_i) = \frac{1}{Z} \exp\left(-\gamma \sum_{j \in \mathcal{N}_i} I(c_i, c_j)\right), \quad (21)
$$

where Z is a normalizing constant, γ controls the degree of spatial smoothing, $\mathcal{N}_i$ denotes a 3×3 neighborhood, and

$$
I(c_i, c_j) = \begin{cases} 0, & c_i = c_j \\ 1, & c_i \neq c_j \end{cases} \quad (22)
$$

Now, let $\mathcal{G}_{i,spatial} = \log\{P(c_i|c_j; j \in \mathcal{N}_i)\}$ and $\mathcal{G}_{i,data}(\mathbf{x}) = \log\{P(c_i|\mathbf{x})\}$, then we may write the discriminant function as [45]

$$
\mathcal{G}_i(\mathbf{x}) = \mathcal{G}_{i,data}(\mathbf{x}) + \mathcal{G}_{i,spatial}, \quad (23)
$$

Date	Wind speed	Inc.	Description
2011/06/08	3-4 m/s	35°	North Sea, Oil-on-water experiment
2012/06/15	5 m/s [14]	31°	North Sea, Oil-on-water experiment
2013/06/11	Unknown	29°	North Sea, Oil-on-water experiment
2015/06/11	4 m/s	35°	North Sea, Oil-on-water experiment
2015/07/29	Unknown	19°	Baltic Sea
2010/05/08	6.5 m/s	42°	Gulf of Mexico, most likely seepage
2010/05/15	Unknown	30°	Gulf of Mexico, Deepwater horizon accident
2011/08/24	Unknown	32°	Gulf of Mexico, slicks of unknown type
2010/07/14	Unknown	37°	Gulf of Mexico, Deepwater horizon accident
2010/05/15	4-7 m/s	30°	Gulf of Mexico, Deepwater horizon accident
2016/07/22	Unknown	40°	Baltic Sea, most likely lookalikes
2008/12/05	Unknown	30°	North Sea, slicks of unknown type
2016/06/15	2-4.5 m/s	41°	North Sea, oil-on-water experiment
2011/06/08	3-4 m/s	47°	North Sea, oil-on-water experiment
2012/11/30	Unknown	30°	Mediterranean Sea, slicks of unknown type

TABLE I: Radarsat-2 quad-pol images evaluated. All images have a single-look resolution (range $\times$ azimuth) of 5.2×7.5 m. The first five images are training images, and the remaining 10 images are test images.

(a) RS2, 8 June 2011 (b) RS2, 15 June 2012 (c) RS2, 11 June 2013

(d) RS2, 11 June 2015 (e) RS2, 29 July 2015

Fig. 1: The Radarsat-2 training data. The images are constructed from the Stokes g_0 features. From the images, features values are selected from areas corresponding to clean sea (cyan), lookalike (blue), plant oil (green), emulsion (yellow) and crude oil (red).

and choose the class corresponding to the largest $\mathcal{G}_i(\mathbf{x})$. The optimal class configuration can be found using the iterated conditional modes algorithm [50]. Several values of the smoothing parameter γ were evaluated for a fixed classifier. The classification results were not highly sensitive to the selected value, and we found a value of 1.5 to provide visual appealing results.

IV. EXPERIMENTS AND RESULTS

We now evaluate the performance of the proposed ocean slick classifiers for hybrid-polarimetric SAR data discussed in Sec. II.

A. Datasets

The Radarsat-2 dataset consists of 15 different quad-pol images covering various areas, oil types, incident angles, and wind conditions (Tab. I). If not stated otherwise, 9×9 multi-looking is used for all images. If in-situ wind measurements are available, this has been reported. Otherwise, if model based wind direction is available and the SAR image is not infested with surface slicks, the wind field is estimated from the SAR image using the CMOD5 algorithm [51], with the wind field direction extracted from the HIRLAM wind model.

The training data consists of five images (Fig. 1) covering the oil-on-water experiments conducted by the Norwegian Clean Seas Association for Operating Companies (NOFO) in 2011 [14], 2012 [14], 2013 [52] and 2015 [53], and one image from the Baltic Sea.

In the NOFO 2011 experiment (Fig. 2a), emulsion, plant oil, and crude oil were released 29, 13, and 9 h before the
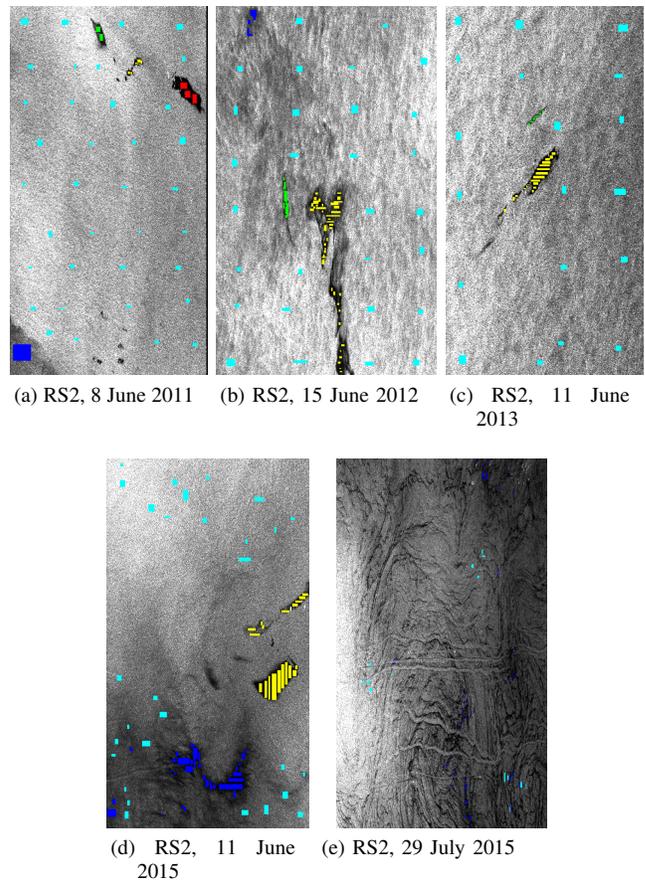
SAR image was acquired, respectively. The dark areas in the upper part of the Stokes g_0 feature image correspond to three different oil slicks. The leftmost slick is plant oil, the middle slick is emulsion, and the rightmost slick is crude oil. Of these oil types, the crude oil has the thickest consistency. The dark area at the lower left corner is most likely caused by very calm sea (wind speed estimated to 2 m/s), and the dark small patches at the lower center part are of unknown origin. Clearly, all oil slicks and lookalikes show high contrast to the surrounding sea water in the g_0 image, despite the very low wind measured. In the NOFO 2012 experiment (Fig. 3a), plant oil was released 14 h before image acquisition, and emulsion was released in four batches 22, 17, 14, and 1 h before SAR image acquisition. The dark spot in the center lower part of the image corresponds to the emulsion discharge. The slick to the left of the major emulsion slick is plant oil. The dark area in the upper left part of the g_0 image is calm sea caused by low wind. For the oil-on-water experiments conducted in June 2013 (Fig. 4a) and June 2015 (Fig. 1d), emulsion and plant oil was released [52], [53]. The last training image is from the Baltic Sea. The slicks observed in this image (Fig. 1e) are typical lookalikes that often occur in the Baltic Sea due to biogenic materials

	all	clean sea	lookalike	plant	emulsion	crude
7 × 7	27 461	13 645	6 578	608	5 993	636
9 × 9	13 263	8 230	4 017	355	3 274	387

TABLE II: Number of training data samples for each of the surface types clean sea, look alike, plant oil, emulsion and crude oil.

		Clean sea	Mineral oil	Plant oil	Class. error
RF	Clean sea	11742	479	26	0.041
	Mineral oil	750	2857	54	0.22
	Plant oil	105	189	61	0.83
XGB	Clean sea	11714	509	24	0.044
	Mineral oil	717	2889	55	0.21
	Plant oil	111	183	61	0.83

TABLE IV: Confusion matrix corresponding to 9×9 looks for both RF (top) and XGB (bottom) classifiers based on 10-fold cross-validation of the training data. The classes clean sea and lookalike are merged.

like e.g. algae or cyanobacteria blooms.

The test data consist of 10 images covering the North Sea, Gulf of Mexico, the Baltic Sea and the Mediterranean Sea (Tab. I). In the 8 May 2010 Gulf of Mexico image (Fig. 5a), the dark slicks are due to oil [10]. Please note that oil in this image is caused by seepage from the bottom of the ocean and not a discharge onto the sea surface (as for the oil-on-water experiment images). The Gulf of Mexico images from 2010 contain oil slicks caused by the Deep Water Horizon accident, whereas the image from 2011 contain slicks of unknown origin. The SAR image from the Baltic Sea on 22 July 2016 (Fig. 10a) contains slicks of unknown origin, but are most likely caused by biogenic materials or low wind. The SAR image from the North Sea on 5 December 2008 (Fig. 11a) contains some ocean slicks of unknown origin. In the NOFO 2016 experiment, emulsion oil was released in several batches, and a Radarsat-2 quad-pol image was acquired on 15 June 2016 (Fig. 12a). The large dark slick is caused by emulsion oil released seven hours before the acquisition [54]. In addition to the training image from the NOFO-2011 experiment, another SAR image (Fig. 13a) was acquired 11 hours before the training image, and contains two slicks. The slick to the left is due to plant oil, released about 2 h before image acquisition, and the slick to the right is caused by a release of emulsion 2 h and 18 h before the satellite pass [55]. Wind speed measurements of 1.6 - 3.3m/s were collected from vessels on site close in time to the satellite passes; however, SAR derived wind speeds suggest larger local variation including occurrences of higher wind speeds. The SAR image from the Mediterranean Sea (Fig. 14a) cover slicks of unknown origin, but that are most likely lookalikes.

Hybrid-polarimetric SAR data was simulated from the Radarsat-2 quad-pol images by first transforming the digital numbers (stored in the *imagery_XY.tif* file), DN, to sigma-naught backscattering coefficients S_{xy} using the attached look-up tables (stored in *lutSigma.xml*), G, using the following relation

$$S_{xy} = DN/G. \tag{24}$$

Then, the hybrid-polarimetric scattering coefficients were simulated using Eqs. (10) and (11).

B. Training the classifiers

The classifiers were trained using SAR data extracted from the five training images (Tab. I), where samples corresponding to clean sea, lookalike, plant oil, emulsion and crude oil were selected (Fig. 1). The number of training pixels depends on the number of looks (Tab. II).

First the image was pre-processed, then features were computed and transformed using domain adaptation strategies.

Feature values corresponding to lookalikes, three oil slick types, and clean sea were extracted and used to train the classifiers.

C. Evaluation

To evaluate the performance of the random forest and extreme gradient boosting classifiers we computed the average correct classification rates for five different feature sets (coherence, covariance, Stokes, extended and RV & RH), two different multilooking strategies (7×7 and 9×9) and three different domain adaptation strategies (normal-transformation, mode scaling and zero-mean, unit-variance transformation) using 10-fold cross-validation on the training data (Tab. III). From the table we see that RF and XGBoost provide similar performance metrics, for all feature sets and multilooking strategies. Coherence and extended were the best feature sets, and the mode scaling was the overall best domain adaptation strategy. The best performance (0.86) was obtained using the extended feature set, 9×9 multilooking, mode scaling domain adaptation, and XBG classifier.

A closer inspection of the performance of the RF classifier using the extended feature set and the zero-mean, unit-variance domain adaptation showed that the classifier struggles to separate plant oil from mineral oil and clean sea for both 9×9 looks (Tab. IV). A similar performance was observed for the XGBoost classifier.

To further assess the performance, we inspected the images of predicted oil type and corresponding confidence based the random forest classifier, extended feature set, 9x9 multilooking, and zero-mean unit-variance domain adaptation strategy (Figs. 2 - 14). The color codes for the class maps are: clean sea (light blue), lookalike (dark blue), plant oil (green), and mineral oil (the transition yellow-orange-red). For mineral oil codes, red indicates a classification with highest confidence, and yellow lowest. The confidence maps are coded according to the color bar to the right of the maps in Fig. 2, with white indicating the highest confidence (probability equal to one), followed by the rainbow colors from red to purple, and black indicating the lowest confidence (probability equal to zero).

For the training images corresponding to the NOFO experiments in 2011 (Fig. 2), 2012 (Fig. 3) and 2013 (Fig. 4). We see that mineral oil is correctly identified. However, edges of mineral oil slick tend to be classified as lookalike (Figs. 2 - 3). For plant oil slicks, parts of the slicks are classified as mineral oil (Figs. 2 - 3) or lookalike (Fig. 4). From the corresponding confidence images, we observed that clean sea was correctly

		Coherence		Covariance		Stokes		Extended		RV and RH	
		RF	XGBoost	RF	XGBoost	RF	XGBoost	RF	XGBoost	RF	XGBoost
7×7	Norm-trans	0.80	0.80	0.81	0.82	0.81	0.82	0.81	0.82	0.76	0.79
	Mode scaling	0.77	0.78	0.79	0.80	0.79	0.79	0.83	0.83	0.73	0.76
	Zero-mean	0.82	0.82	0.81	0.82	0.82	0.82	0.82	0.83	0.77	0.79
9×9	Norm-trans	0.81	0.82	0.84	0.84	0.84	0.84	0.84	0.84	0.78	0.80
	Mode scaling	0.81	0.82	0.84	0.84	0.84	0.84	0.85	0.86	0.73	0.75
	Zero-mean	0.83	0.84	0.84	0.84	0.84	0.84	0.84	0.85	0.78	0.80

TABLE III: Average correct classification rates for random forest and extreme gradient boosting machine estimated using 10-fold cross-validation on the training feature vectors.

(a) D_{11} feature image

(b) Classified image

(c) Confidence image

Fig. 2: North Sea, oil spill experiment, 8 June 2011. Evaluation of the Random Forest classifier and corresponding confidence image. CL data simulated from Radarsat-2 quad-pol (product id SAR-PF-1307733525, image id 137348).

(a) D_{11} feature image

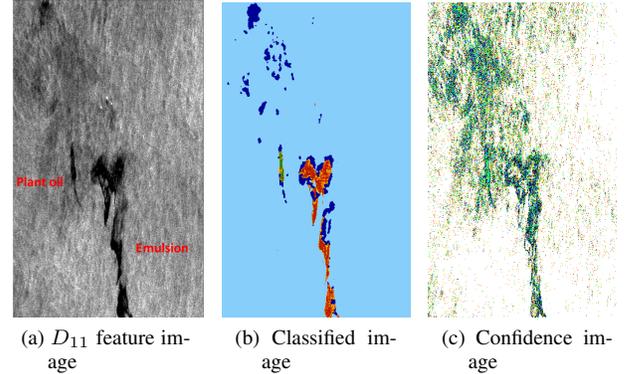(b) Classified image

(c) Confidence image

Fig. 3: North Sea, oil spill experiment, 15 June 2012. Evaluation of the Random Forest classifier and corresponding confidence image. CL data simulated from Radarsat-2 quad-pol (product id SAR-PF-1353064508, image id 202391).

(a) D_{11} feature image

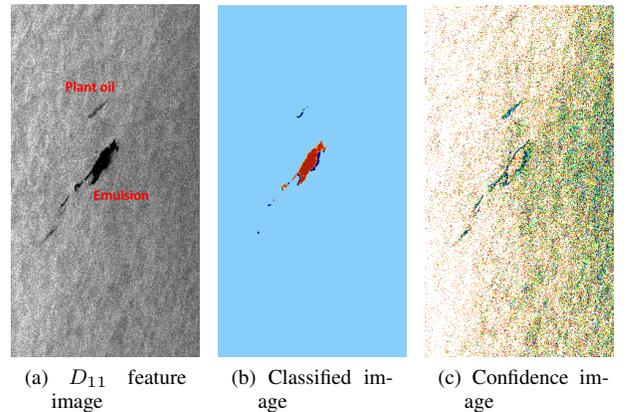(b) Classified image

(c) Confidence image

Fig. 4: North Sea, oil spill experiment, 11 June 2013. Evaluation of the Random Forest classifier and corresponding confidence image. CL data simulated from Radarsat-2 quad-pol (product id SAR-PF-1372058111, image id 264873).

classified with high confidence, the same is a large mineral oil slick in the NOFO 2011 experiment (Fig. 3). However, plant oil slicks are assigned a lower confidence, as well as the edges of the mineral oil slicks.

In order to evaluate the potential to classify surface slicks in new SAR data, obtained at different times and locations, we classify the 10 test images. For most of the images the algorithm provides correct classification (Figs. 5, 6, 8, 10, 11, 12, and 14). Three of these images are from the Gulf of Mexico and contain mineral oil (Figs. 5, 6, 8), two images contains, most likely, lookalikes (Figs. 10 and 14), and one image contain, most likely, release of emulsion or produced water (Fig. 11). For the NOFO-2011 image, the classifier was able to identify the emulsion slick, but mis-classified the plant oil slick as emulsion (Fig. 13).

The confidence maps gave similar results as for the training images. Clean sea pixels were classified with highest confidence, whereas surface slicks were classified with lower confidence, with the exception of the large slicks in the Gulf of Mexico images (Figs. 5, 8, and 9).

V. DISCUSSION AND CONCLUSIONS

In this paper, we have utilized the structure of compact polarimetry CL-mode data to classify ocean surface slicks. Several feature sets, classifiers, domain adaptation strategies and multilooking strategies were investigated and applied to hybrid-polarimetric SAR data simulated from Radarsat-2 quad-pol data covering oil-on-water exercises and other slicks in the North Sea, the Deepwater Horizon incident and seepages in the Gulf of Mexico, biogenic slicks in the Baltic Sea, and lookalikes in the Mediterranean Sea. The feature sets, classifiers, domain adaptation strategies and multilooking strategies were first evaluated by 10-fold cross-validation on the training dataset (Tab. III). The results show that the XGBoost and RF classifiers have similar performance for a given feature set and domain adaptation strategy. The coherency and extended feature sets were the best feature sets, whereas the RV and RH feature set was the worst. Regarding the multilooking strategy, 9×9 was better than 7×7 (Tab. III). The overall

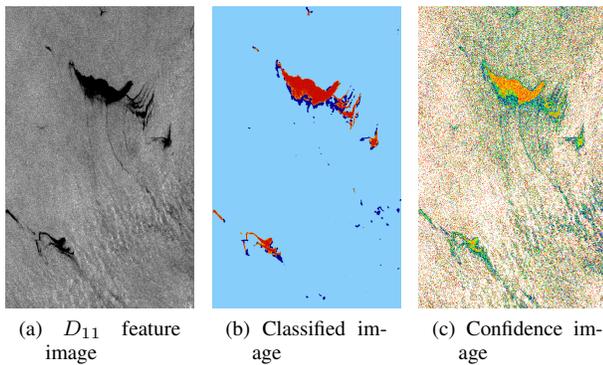(a) D_{11} feature image   (b) Classified image   (c) Confidence image

Fig. 5: Gulf of Mexico, most likely natural oil seepage, 8 May 2010. Evaluation of the Random Forest classifier and corresponding confidence image. CL data simulated from Radarsat-2 quad-pol (product id PDS 02279950, image id 80536). RADARSAT-2 Data and Products MacDonald, Dettwiler and Associates Ltd. (2010)-All Rights Reserved.
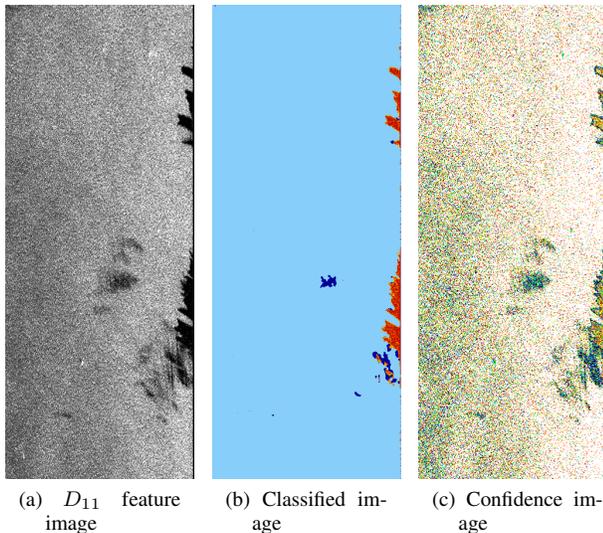

(a) D_{11} feature image   (b) Classified image   (c) Confidence image

Fig. 6: Gulf of Mexico, part of the Deepwater Horizon oil spill, 15 May 2010. Evaluation of the Random Forest classifier and corresponding confidence image. CL data simulated from Radarsat-2 quad-pol (product id PDS-03394960, image id 81514).

(a) D_{11} feature image   (b) Classified image   (c) Confidence image
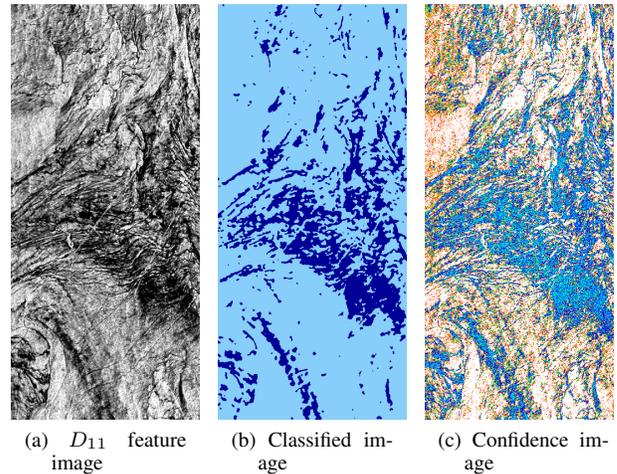
Fig. 7: Gulf of Mexico, 24 August 2011. Evaluation of the Random Forest classifier and corresponding confidence image. CL data simulated from Radarsat-2 quad-pol (product id PDS-03399810, image id 150628).

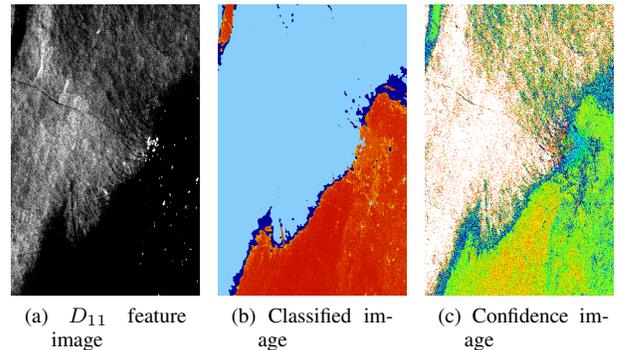(a) D_{11} feature image   (b) Classified image   (c) Confidence image

Fig. 8: Gulf of Mexico, 14 July 2010. Evaluation of the Random Forest classifier and corresponding confidence image. CL data simulated from Radarsat-2 quad-pol (product id PDS-03380580, image id 89577).
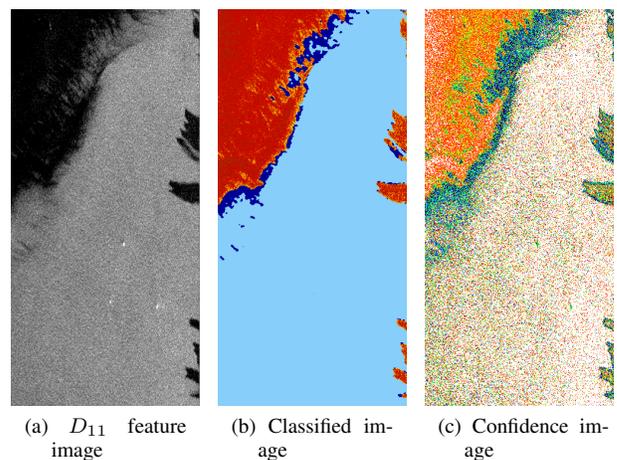

(a) D_{11} feature image   (b) Classified image   (c) Confidence image

Fig. 9: Gult of Mexico, 15 May 2010. Evaluation of the Random Forest classifier and corresponding confidence image. CL data simulated from Radarsat-2 quad-pol (product id PDS-02279960, image id 81514).

best domain adaptation strategy was zero-mean, unit-variance transformation.

Based on the cross-validation results we selected the random forest classifier, the extended feature set, and the zero-mean, unit-variance domain adaptation strategy, 9×9 multilooking, and performed a visual evaluation on new image data (Figs. 5 - 14). For all mineral oil slicks we observed that the edges tended to be classified as lookalike. A similar observation was observed by Skrunes et al. [14], which explained this phenomenon as: "...zone around the edges of the emulsion and crude oil may be a thinner film, with properties more similar to the plant oil slick". Another contribution to this phenomenon are edge effects since edge pixels are smoothed during the imaging and multi-looking process.

The study showed that using features that utilized the

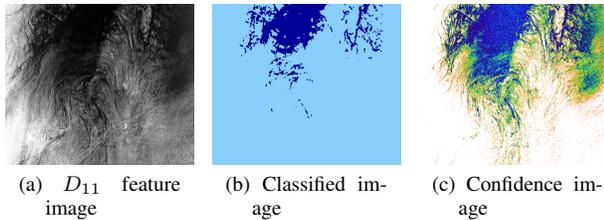(a) D_{11} feature image   (b) Classified image   (c) Confidence image

Fig. 10: Baltic Sea, 22 July 2016. Evaluation of the Random Forest classifier and corresponding confidence image. CL data simulated from Radarsat-2 quad-pol (product id SAR-PF-1469378004, image id 493295).
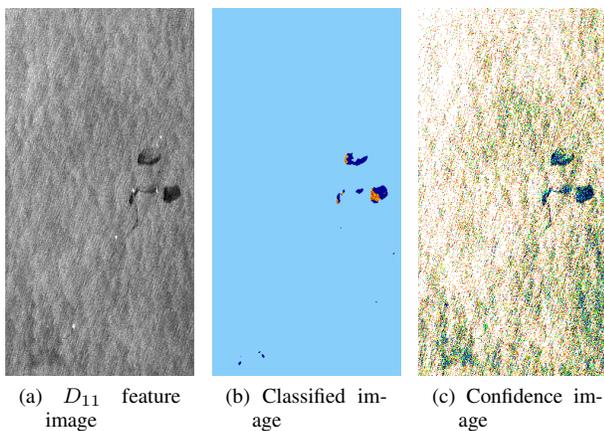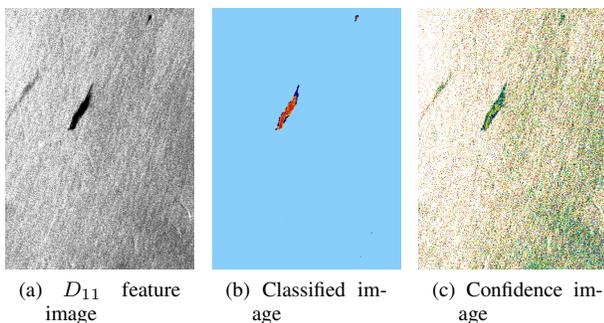

(a) D_{11} feature image   (b) Classified image   (c) Confidence image

Fig. 11: North Sea, slicks of unknown type, 5 December 2008. Evaluation of the Random Forest classifier and corresponding confidence image. CL data simulated from Radarsat-2 quad-pol (product id SAR-PF-1353063396, image id 23047).

(a) D_{11} feature image   (b) Classified image   (c) Confidence image

Fig. 12: North Sea, oil spill experiment, 15 June 2016. Evaluation of the Random Forest classifier and corresponding confidence image. CL data simulated from Radarsat-2 quad-pol (product id SAR-PF-1466180514, image id 484959). (a)-(c) feature images, (d) classification image, and (e) confidence image.
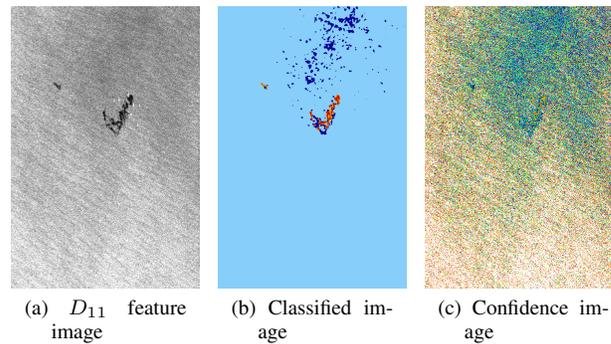

(a) D_{11} feature image   (b) Classified image   (c) Confidence image

Fig. 13: North Sea, oil spill experiment, 8 June 2011. Evaluation of the Random Forest classifier and corresponding confidence image. CL data simulated from Radarsat-2 quad-pol (product id SAR-PF-1336132931, image id 137269).

(a) D_{11} feature image   (b) Classified image   (c) Confidence image
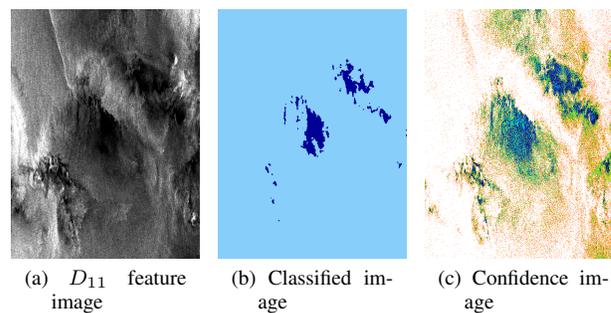
Fig. 14: Mediterranean Sea, slicks of unknown origin, 30 November 2012. Evaluation of the Random Forest classifier and corresponding confidence image. CL data simulated from Radarsat-2 quad-pol (product id PDS-03441350, image id 231822).

phase information between channels information (Coherence, Correlation, Stokes, and Extended) provide better performance than using features that were only based on the amplitude values (RV and RH). Similar findings were found for the co-polarized phase difference in quad-pol data [4], [5], [11], [13], [15]. Even though the phase information between the channels improved the classification accuracy, there is still discriminative information in the amplitude values. Using the RV and RV feature set, we achieved a classification accuracy of 80%. Hence, we expect there that ground range detected (GRD) products will, to some degree, be able to distinguish the oil types from each other.

A key component of the proposed system is the domain adaptation that aims to transform the test image into the same distribution as the training data. This processing step, and the quality of domain adapation algorithm, is crucial since both the wind level and incidence angle alter the amplitude level of the backscattered signal. However, the same restrictions on the detectability with respect to the wind level (i.e. between 3 - 10 m/s) and incidence angle (i.e. between $20°$ and $45°$) are expected as for single-pol images. A central and critical component of the domain adaptation module is the automatic extraction of clean sea pixels. In our study, we based the clean sea mapping on the conformity coefficient, which has the

property that pixels values less than zero corresponds to slicks [8], [10]. However, other measures that are not too sensitive to the wind level may also be used [17]. Cases when the image is infested with slicks (e.g. Figs. 7, 8 and 10) are challenging, since we risk that the main peak of the image histogram does not represent clean sea. For such cases a check that only pixels corresponding to positive conformity values are selected may be applied.

Given high resolution wind speed and direction estimates, we may model the radar backscatter from the ocean surface using models like CMOD5 [51]. By comparing the observed background intensities with the modelled ones, reduced backscatter values with respect to clean sea are expected in the presence of oil slicks. Such approach has been utilized for detecting cyanobacteria blooms in the Curonia Lagoon [56]. However, this approach relies on high resolution wind estimates, which is not available in this study, and the CMOD5 model is developed for VV-polarization. If wind information with sufficient resolution is available, this approach is interesting for further work, in particular in combination with a CMOD5 extension for hybrid-polarimetric SAR data [57].

A training dataset of only 5 images is critically low for training the RF and XGB classifiers. In order to capture image variation caused by changing weather situations, different oil types, different incident angles, the time the oil has been situated in the water, etc., a much larger training dataset is desirable.

Although the tests are performed on a limited sample of images, the findings demonstrate, as in [17], [18] and [22], that the hybrid-polarimetric SAR has great potential in oil slick monitoring and may, in many cases, provide results comparable to those obtained by quad-polarimetric sensors. In our study we simulated the hybrid-polarimetric mode from quad-pol data. As in Raney [23], we expect that a similar performance is obtained for true hybrid-polarimetric images, given that the single-look complex image is available. If the only detected products are available, the performance is expected to be lower, as shown in Tab. III.

The several planned Earth-observing satellite missions supporting compact polarimetry will provide the increased swath possibilities necessary for operational oil spill detection. With the potential performance enhancement in terms of lookalike suppression demonstrated in this analysis, we expect that SAR systems providing compact polarimetry modes will have a high impact on operational oil slick monitoring in the future given that spatial- and temporal coverage is high enough and single-look complex images are provided.

VI. ACKNOWLEDGEMENTS

REFERENCES

[1] I. S. Robinson, *Measuring the Ocean from Space: The Principles and Methods of Satellite Oceanography.* Berlin: Springer, 2004.

[2] D. Geudtner, R. Torres, P. Snoeij, M. Davidson, and B. Rommen, "Sentinel-1 system capabilities and applications," in *2014 IEEE Geosci. Remote Sensing Symp.*, July 2014, pp. 1457–1460.

[3] S. V. Nghiem, S. H. Yueh, R. Kwok, and F. K. Li, "Symmetry properties in polarimetric remote sensing," *Radio Science*, vol. 27, no. 5, pp. 693–711, 1992.

[4] M. Migliaccio, F. Nunziata, and A. Gambardella, "On the co-polarized phase difference for oil spill observation," *Int. J. Remote Sensing*, vol. 30, no. 6, pp. 1587–1602, 2009.

[5] D. Velotto, M. Migliaccio, F. Nunziata, and S. Lehner, "Dual-polarized TerraSAR-X data for oil-spill observation," *IEEE. Trans. Geosci. Remote Sensing*, vol. 49, no. 12, pp. 4751–4762, 2011.

[6] M. Gade, W. Alpers, H. Masuko, and T. Kobayashi, "Imaging of biogenic and anthropogenic ocean surface films by the multifrequency/multipolarization SIR-C/X-SAR," *J. Geophysical Research*, vol. 103, no. C), pp. 18 851–18 866, 1998.

[7] P. Lombardo and C. J. Oliver, "Optimum detection and segmentation of oil-slicks using polarimetric SAR data," *IEE Proc. -Radar, Sonar Navig.*, vol. 147, no. 6, pp. 309–321, 2000.

[8] F. Nunziata, A. Gabardella, and M. Migliaccio, "On the Mueller scattering matrix for SAR sea oil slick observation," *IEEE Geosci. Remote Sens. Lett.*, vol. 5, no. 4, pp. 691–695, 2008.

[9] M. Migliaccio, A. Gambardella, F. Nunziata, M. Shimada, and O. Isoguchi, "The PALSAR polarimetric mode for sea oil observation," *IEEE Trans. Geosci. Remote Sens.*, vol. 47, no. 12, pp. 4032–4041, 2009.

[10] B. Zhang, W. Perrie, X. Li, and W. G. Pichel, "Mapping sea surface oil slicks using Radarsat-2 quad-polarization SAR image," *Geophys. Res. Lett.*, vol. 38, 2011.

[11] M. Migliaccio, F. Nunziata, A. Montuori, X. Li, and W. G. Pichel, "A multifrequency polarimetric SAR processing chain to observe oil fields in the Gulf of Mexico," *IEEE Trans. Geosci. Remote Sens.*, vol. 49, no. 12, pp. 4729–4737, 2011.

[12] M. Migliaccio, F. Nunziata, and A. Buono, "A review on SAR polarimetry for sea oil slick observations," *Int. J. Remote Sensing*, vol. 36, no. 12, pp. 3243–3273, 2015.

[13] M. Migliaccio, A. Gambardella, and M. Tranfaglia, "SAR polarimetry to observe oil spills," *IEEE Trans. Geosci. Remote Sensing*, vol. 45, no. 2, pp. 506–511, 2007.

[14] S. Skrunes, C. Brekke, and T. Eltoft, "Characterization of marine surface slicks by Radarsat-2 multipolarization features," *IEEE Trans. Geosci. Remote Sens.*, vol. 52, no. 9, pp. 5302–5319, 2014.

[15] S. Singha, R. Ressel, and S. Lehner, "Multi-frequency and multipolarization analysis of oil slicks using TerraSAR-X and RADARSAT-2 data," in *2016 IEEE Int. Geosci.Remote Sensing Symp. (IGARSS)*, 2016, pp. 4035–4038.

[16] ——, "Investigations into the X and C band quad-pol features for oil slick characterization," in *Proc. EUSAR 2016: 11th European Conf. Synthetic Aperture Radar*, 2016, pp. 1–4.

[17] A. B. Salberg, Ø. Rudjord, and A. H. S. Solberg, "Oil spill detection in hybrid-polarimetric SAR images," *IEEE Trans. Geosci. Remote Sens.*, vol. 52, no. 10, pp. 6521–6533, 2014.

[18] R. Shirvany, M. Chabert, and J. Tourneret, "Ship and oil-spill detection using the degree of polarization in linear and hybrid/compact dual-pol SAR," *IEEE J. Selected Topics Applied Earth Observations Remote Sensing*, vol. 5, no. 3, pp. 885–892, 2012.

[19] R. K. Raney, "A perspective on compact polarimetry," *IEEE Geosci. Remote Sens. Newslett.*, vol. 160, pp. 12–18, Sep. 2011.

[20] M. E. Nord, T. L. Ainsworth, J. Lee, and N. J. S. Stacy, "Comparison of compact polarimetric synthetic aperture radar modes," *IEEE Trans. Geosci. Remote Sens.*, vol. 47, no. 1, pp. 174–188, 2009.

[21] P. C. Dubois-Fernandez, J. Souyris, S. Angelliaume, and F. Garestier, "The compact polarimetry alternative for spaceborne SAR at low frequency," *IEEE Trans. Geosci. Remote Sens.*, vol. 46, no. 10, pp. 3208–3222, 2008.

[22] J. Souyris, P. Imbo, R. Fjørtoft, S. Mingot, and J. Lee, "Compact polarimetry based on symmetry properties of geophysical media: The $\pi/4$ mode," *IEEE Trans. Geosci. Remote Sens.*, vol. 43, no. 3, pp. 634–646, 2005.

[23] R. K. Raney, "Hybrid-polarity SAR architecture," *IEEE Trans Geosci. Remote Sens.*, vol. 45, no. 11, pp. 3397–3404, 2007.

[24] A. Buono, F. Nunziata, M. Migliaccio, and X. Li, "Polarimetric analysis of compact-polarimetry SAR architectures for sea oil slick observation,"

IEEE Trans. Geosci. Remote Sensing, vol. 54, no. 10, pp. 5862–5874, 2016.

[25] L. J. V. Kumar, J. K. Kishore, and P. K. Rao, "Decomposition methods for detection of oil spills based on Risat-1 SAR images," *Int. J. Remote Sensing Geosci.*, vol. 3, no. 4, pp. 1–10, 2014.

[26] G. E. Atteia and M. J. Collins, "On the use of compact polarimetry SAR for ship detection," *ISPRS J. Photogramm. Remote Sens.*, vol. 80, pp. 1–9, June 2013.

[27] M. Denbina and M. J. Collins, "Iceberg detection using compact polarimetric synthetic aperture radar," *Atmosphere-Ocean*, vol. 50, no. 4, pp. 437–446, 2012.

[28] C. Brekke and A. H. S. Solberg, "Oil spill detection by satellite remote sensing," *Remote Sensing Environment*, vol. 95, no. 1, pp. 1–13, 2005.

[29] G. R. Valenzuela, "Theories for the interaction of electromagnetic and ocean waves – A review," *Boundary-Layer Meteorol.*, vol. 13, no. 1–4, pp. 61–85, 1978.

[30] B. Minchew, C. E. Jones, and B. Holt, "Polarimetric analysis of backscatter from the Deepwater Horizon oil spill using L-band synthetic apeture radar," *IEEE Trans. Geosci. Remote Sensing*, vol. 50, no. 10, pp. 3812–3830, 2012.

[31] T. Elfouhaily, D. R. Thompson, and D. Vandemark, "A new bistatic model for electromagnetic scattering from perfectly conducting random surfaces," *Waves Random Media*, vol. 9, pp. 281–294, 1999.

[32] J. Lee, D. L. Schuler, and T. L. Ainsworth, "Polarimetric SAR data compensation for terrain azimuth slope variation," *IEEE Trans Geosci. Remote Sens.*, vol. 38, no. 5, pp. 2153–2163, 2000.

[33] A. Iodice, A. Natale, and D. Riccio, "Retrieval of soil surface parameters via a polarimetric two-scale model," *IEEE Trans Geosci. Remote Sens.*, vol. 49, no. 7, pp. 2531–2547, 2011.

[34] W. R. Alpers, D. B. Ross, and C. L. Rufenach, "On the detectability of ocean surface waves by real and synthetic aperture radar," *J. Geophys. Res.*, vol. 86, no. C7, pp. 6481–6498, 1981.

[35] B. Minchew, "Determining the mixing of oil and sea water using polarimetric synthetic aperture radar," *Geophys. Res. Lett.*, vol. 39, no. L16607, doi:10.1029/2012GL052304, p. 6 pp., 2012.

[36] D. Tuia, C. Persello, and L. Bruzzone, "Domain adaptation for the classification of remote sensing data: An overview of recent advances," *IEEE Geosci. Remote Sens. Mag.*, vol. 4, no. 2, pp. 41–57, 2016.

[37] L. Bruzzone and D. F. Prieto, "Unsupervised retraining of a maximum likelihood classifier for the analysis of multitemporal remote sensing images," *IEEE Trans. Geosci. Remote Sensing*, vol. 39, no. 2, pp. 456–460, 2001.

[38] A. B. Salberg, "Retraining maximum likelihood classifiers using a low-rank model," in *Proc. 2011 IEEE Int. Geosci. Remote Sensing Symp.*, Vancouver, Canada, July 2011, pp. 166–169.

[39] L. Bruzzone and M. Marconcini, "Toward the automatic updating of land-cover maps by a domain-adaptation SVM classifier and a circular validation strategy," *IEEE Trans. Geosci. Remote Sens.*, vol. 47, no. 4, pp. 1108–1122, 2009.

[40] S. Skrunes, C. Brekke, and A. P. Doulgeris, "Characterization of low-backscatter ocean features in dual-copolarization SAR using log-cumulants," *IEEE Geosci. Remote Sens. Lett.*, vol. 12, no. 4, pp. 836–840, 2015.

[41] S. R. Cloude, "Compact decomposition theory," *IEEE Geosci. Remote Sens. Lett.*, vol. 9, no. 1, pp. 28–32, 2012.

[42] J. Kittler and J. Illingworth, "Minimum error thresholding," *Pattern Recognition*, vol. 19, no. 1, pp. 41–47, 1986.

[43] B. Storvik, G. Storvik, and R. Fjørtoft, "On the combination of multisensor data using meta-Gaussian distributions," *IEEE Trans. Geosci. Remote Sens.*, vol. 47, no. 7, pp. 2372–2379, 2009.

[44] B. W. Silverman, *Density estimation for statistics and data analysis*. London: Chapman and Hall, 1986.

[45] A. H. S. Solberg, "Flexible nonlinear contextual classification," *Pattern Recognition Lett.*, vol. 25, pp. 1501–1508, 2004.

[46] L. Breiman, "Random forests," *Machine Learning*, vol. 45, pp. 5–32, 2001.

[47] T. Chen and C. Guestrin, "XGBoost: A scalable tree boosting system," in *Proc. 22nd ACM SIGKDD Int. Conf. Knowledge Discovery and Data Mining*, New York, 2016, pp. 785–794.

[48] T. Hastie, R. Tibshirani, and J. Friedman, *The Elements of Statistical Learning: Data Mining, Inference, and Prediction*, 2nd ed.   New York: Springer, 2009.

[49] L. Loosvelt, J. Peters, H. Skriver, H. Lievens, F. M. B. Van Coillie, B. De Baets, and N. E. C. Verhoest, "Random forest as a tool for estimating uncertainty at pixel-leel in SAR image classification," *Int. J. Appl. Earth Obs. Geoinfo.*, vol. 19, pp. 173–184, 2012.

[50] J. Besag, "On the statistical analysis of dirty pictures," *J. R. Statist. Soc. B*, vol. 48, no. 3, pp. 259–302, 1986.

[51] H. Hersbach, A. Stoffelen, and S. de Haan, "An improved C-band scatterometer ocean geophysical model function: CMOD5," *J. Geophys. Res.*, vol. 112, no. C03006, 2007.

[52] NOFO, "Oil spill response exercise. oil on water 2013," The Norwegian Clean Seas Association For Operating Companies/The Norwegian Coastal Administration, Tech. Rep., 2013.

[53] ——, "Oil on water 2015 (in norwegian)," The Norwegian Clean Seas Association For Operating Companies/The Norwegian Coastal Administration, Tech. Rep., 2015.

[54] ——, "Oil on water 2016 (in norwegian)," The Norwegian Clean Seas Association For Operating Companies/The Norwegian Coastal Administration, Tech. Rep., 2016.

[55] C. Brekke, B. Hold, C. Jones, and S. Skrunes, "Discrimination of oil spills from newly formed sea ice by synthetic aperture radar," *Remote Sensing Environment*, vol. 145, pp. 1–14, 2014.

[56] M. Adamo, E. Matta, M. Bresciani, G. De Carolis, D. Vaiciute, C. Giardino, and G. Pasquariello, "On the synergistic use of SAR and optical imagery to monitor cyanobacteria blooms: the Curonian Lagoon case study," *European J. Remote Sensing*, vol. 46, pp. 789–805, 2013.

[57] M. Debina and M. Collins, "Wind speed estimation using C-band compact polarimetric SAR for wide swath imaging modes," *ISPRS J. Photogramm. Remote Sensing*, vol. 113, pp. 75–85, 2016.